Q. J. R. Meteorol. Soc. (1994), **120**, pp. 1045–1067 551.513.1

Wave–zonal-flow interaction and ultra-low-frequency variability in a simplified global circulation model

By P. M. JAMES[1]*, K. FRAEDRICH[2] and I. N. JAMES[1]

[1] *University of Reading, UK*
[2] *University of Hamburg, Germany*

(Received 10 March 1993; revised 1 December 1993)

SUMMARY

The interactions between baroclinic waves and the zonal-mean mid-latitude flow are investigated using a multilevel primitive-equation model of moderate resolution with idealized surface friction and diabatic heating terms. Integrations corresponding to 100 years were performed under perpetual solstice conditions. Empirical Orthogonal Function (EOF) analyses were carried out on the zonal-mean zonal wind, $[u]$. Adjustments to the winter hemisphere zonal jet due to the growth and decay of baroclinic waves can be described in terms of the first two EOF patterns, which exhibit substantial interannual variability. For a single lifecycle, such adjustments take the form of a circuit of a phase-space whose axes are defined by the amplitudes of the two EOFs. The cumulative effects of multiple lifecycles lead to a low-frequency circulation in the phase-space, with a timescale of about 150 days. We suggest that this effect may be intrinsically related to the internal generation of ultra-low-frequency variability in the model. Normal-mode lifecycle calculations, including dissipation, reveal similar phase-space properties. The growth rates of normal-mode disturbances are shown to be highly sensitive to the phase of the first EOF.

1. INTRODUCTION

The atmosphere fluctuates on a very wide range of timescales and, in particular, can exhibit considerable variability interannually. Following Madden (1976) and Lorenz (1979), mechanisms for the generation of such variability have usually been classified into two types: those 'internal' or those 'external' to the atmospheric dynamics. Assessing the relative importance of these sources is undoubtedly a crucial question.

James and James (1989) integrated a simplified, moderate-resolution version of a global circulation model (the simplified global circulation model or SGCM), without moist processes or orography, for a period corresponding to 100 years. The simulation generated a red spectrum of variability which extended at least to decadal timescales. They termed fluctuations with timescales longer than a year 'ultra-low-frequency variability' (ULFV).

Recently, James and James (1992) (hereafter referred to as JJ92) have discussed the characteristics of the ULFV in the SGCM in terms of the fluctuations of the mid-latitude zonal jets and identified a principal mode of ULFV. They showed how positive feedbacks might arise between the zonal flow and baroclinic lifecycles growing and decaying on this flow, so that anomalous zonal flows are maintained against dissipation, leading to enhanced low-frequency fluctuations.

Undoubtedly the source of internal mid-latitude tropospheric variability in the SGCM lies with the baroclinically unstable synoptic-scale waves. In this paper, we shall expand further on the work of JJ92 by investigating how the principal modes of variability of the zonal-mean flow are related to changes to this flow generated by growing and decaying baroclinic eddies. The objective will be to determine whether the form of the zonal-mean flow subsequently feeds back onto the growth of eddies so as to generate variability with a timescale much longer than that of the waves themselves.

Section 2 begins with a description of the model integrations that we have carried out. There we shall reiterate the main findings of JJ92, and discuss the principal modes

*Corresponding author: Present address—Meteorologisches Institut, Universität München, Theresienstraße 37, 80333 München, Germany.

of variability of the zonal-mean flow and their temporal characteristics in the current integrations. In section 3, the form of wave–zonal-flow interaction in the model data will be investigated, and the possibilities for a feedback system discussed. In section 4, an alternative approach to the study of wave–zonal-flow interaction using linear normal-mode lifecycle calculations will be presented. This expands on the frictionless, adiabatic lifecycle computations of JJ92 by including parametrizations of dissipative processes. Finally, conclusions will be drawn in section 5.

2. Background: The 100-year SGCM integrations

(*a*) *The model*

The SGCM has been described by James and Gray (1986) and further by JJ92, to which sources the reader requiring further details is referred. In brief summary, the model is run at a moderately low spectral resolution with triangular truncation at wavenumber 21 (T21) in the horizontal, and has five equispaced sigma levels in the vertical. It has no orography, no continents and no moist processes. Dissipative processes are parametrized using linear Rayleigh friction and Newtonian cooling terms, with timescales of one day and 30 days respectively. The model is run in perpetual solstice mode (southern hemisphere winter).

Despite the model's low resolution and simplicity, JJ92 have shown that its mean climatology is surprisingly realistic. Poleward eddy fluxes of heat and momentum in the winter mid latitudes were similar in form and magnitude to those observed, and the winter hemisphere zonal jet exhibited a double maximum, rather like that observed in the southern hemisphere (Hoskins *et al.* 1989).

Two runs have been carried out, each extending to the equivalent of 100 years, with data being archived daily. Run A, carried out precisely as indicated above, is the basic model integration under investigation. Also, so as to isolate the dynamics of the interaction between baroclinic eddies of synoptic scales and the zonal flow, run B was set up as a special experiment in which a seven-fold symmetry was imposed in the meridional direction. Therefore, only wavenumbers 0, 7 and 14 are present in run B and all long waves (small zonal wavenumber) are thereby excluded. Wavenumber 7 was chosen since it is a typical synoptic length scale and is the scale with the fastest growing linear normal modes on the time-mean zonal state. Thus, A and B are reintegrations of runs 1 and 5 of JJ92, but with more frequent archiving of the data.

(*b*) *EOF analysis of the zonal-mean zonal wind*

The time-mean zonal-mean zonal wind, $[\overline{u}]$, fields for runs A and B are shown in Fig. 1. In run A, the double jet structure is clearly visible. A subtropical jet is centred near latitude 27°S and a mid-latitude jet near 47°S. In run B, the winter-hemisphere jet is broader, especially on its poleward side, and there is little evidence of a split jet structure.

Following JJ92, EOF analyses have been carried out on the daily $[u]$-fields from both runs. There are two principal modes of variability of $[u]$, described by the resulting EOF1 and EOF2 patterns. Those for run A are shown in Fig. 2. Centred in the winter mid latitudes, they are a quarter-wave out of phase meridionally with each other, but are otherwise spatially similar. Despite the differences in the climatological $[u]$-fields, the first two EOFs in run A are virtually identical to those of run B, although the latter are centred slightly more equatorwards by about 4 degrees of latitude. The modes account for 32.5% and 13.1% of the variance of $[u]$ in run A, and 32.3% and 22.8% of the variance in run B, respectively.

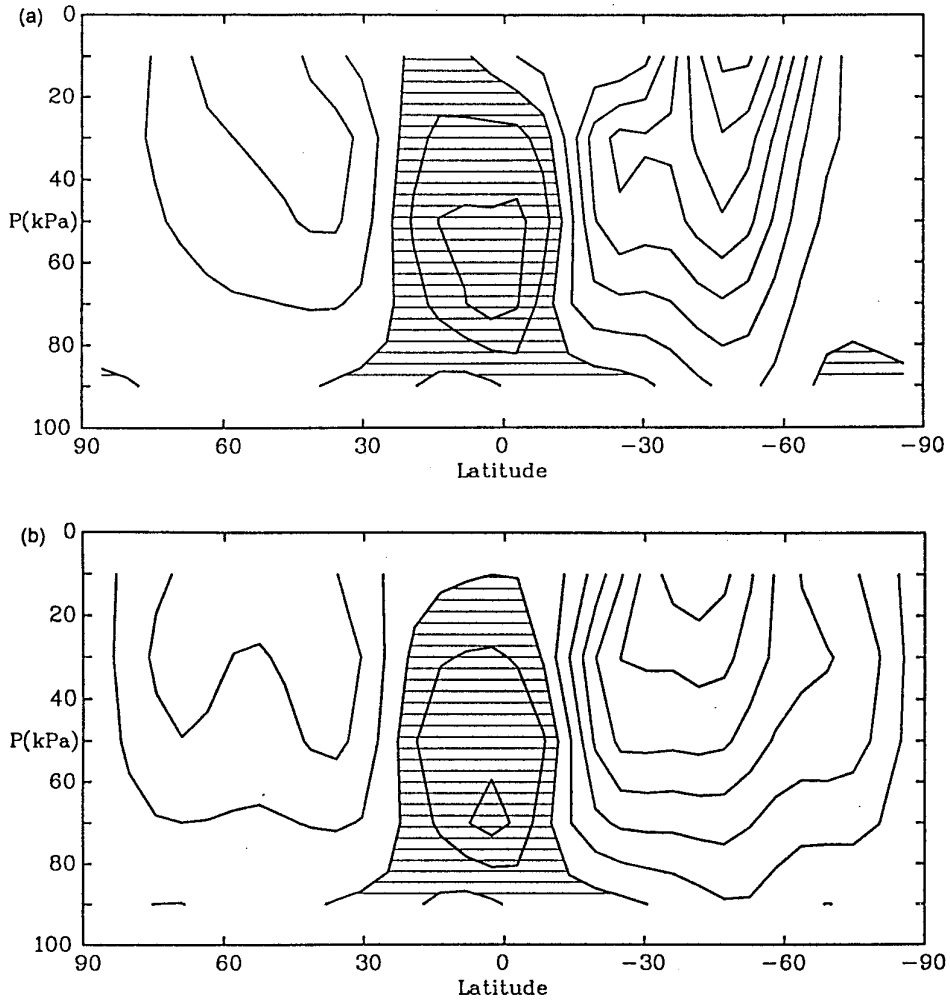

Figure 1. The time-mean zonal-mean zonal wind, $[u]$, constructed from the last 96 years of (a) run A and (b) run B. Contour interval 5 m s^{-1}; easterlies are shaded.

The fluctuations in the winter jets represented by the first two EOFs in run A are illustrated in Fig. 3. The characteristics of these EOFs bear a close resemblance to the principal modes of low-frequency variability of the observed wintertime zonal-mean jets (e.g. Kidson 1988, Nigam 1990).

The EOF1 and EOF2 modes are fundamental for describing variability across a very wide range of timescales. When a low-pass filter with a cut-off at about 60 days is applied to the $[u]$-field in run A, very similar EOF patterns emerge; EOF1 alone accounting for 41% of the variance.

Figure 4(a) shows the frequency spectrum of the last 96 years of the amplitude of EOF1 (principal component, PC1) from run A, showing all timescales of variability from two days to 96 years. The spectrum is red, having a broad maximum of variability at timescales around one to two years. Notable power is still present at decadal timescales. This ULFV is generated purely by internal dynamics. The spectrum of PC2 (not shown) also peaks near a timescale of one to two years, although, in general, it has a less red background than PC1 and somewhat resembles white noise at timescales longer than about 80 days.

Figure 4(b) shows the corresponding PC1 spectrum for run B. Levels of ULFV are very similar to the level in run A. Yet, PC1 has a white spectrum for timescales beyond

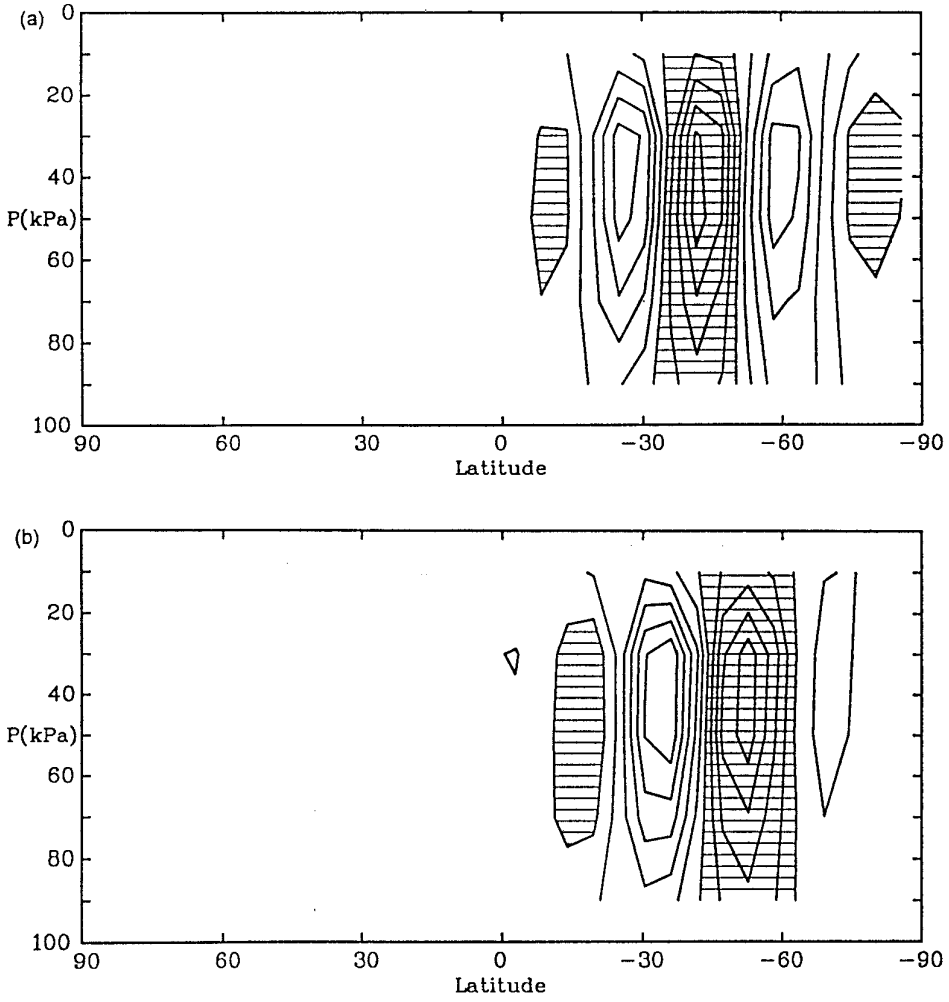

Figure 2. The first two EOFs of $[u]$ for run A, normalized so that the sum of the squares of the gridpoint values is unity. Contour interval 0.06; values below −0.03, shaded. (a) EOF1, (b) EOF2.

about 60 days—reflecting the relatively higher level of synoptic timescale variability in run B. In PC2 (not shown), power tails off slightly after reaching a peak near the 60-day timescale.

Using these basic results as the starting point, we shall now examine the hypothesis that ULFV can arise from feedbacks between baroclinic disturbances and the zonal-mean part of the flow. In particular, the PC time-series will be investigated to reveal the characteristics of such wave–zonal-flow interactions in the SGCM.

3. The nature of wave–zonal-flow interactions in the SGCM

(*a*) *The basic picture of the effect of waves on the zonal flow in run B*

As pointed out by JJ92, the tripole anomaly pattern of $[u]$ in the negative phase of EOF1 bears some resemblance to the adjustment of $[u]$ resulting from the classical baroclinic lifecycle on a mid-latitude zonal jet (Simmons and Hoskins 1978). Following the lifecycle, a westerly anomaly develops, flanked on either side by easterly anomalies. Run B is an ideal test bed for investigating this connection further.

Figure 5 shows latitude–time plots of the mid-level (50 kPa) anomaly fields of $[u]$ and of the corresponding zonal-mean eddy kinetic energy [KE] from run B. The diagrams

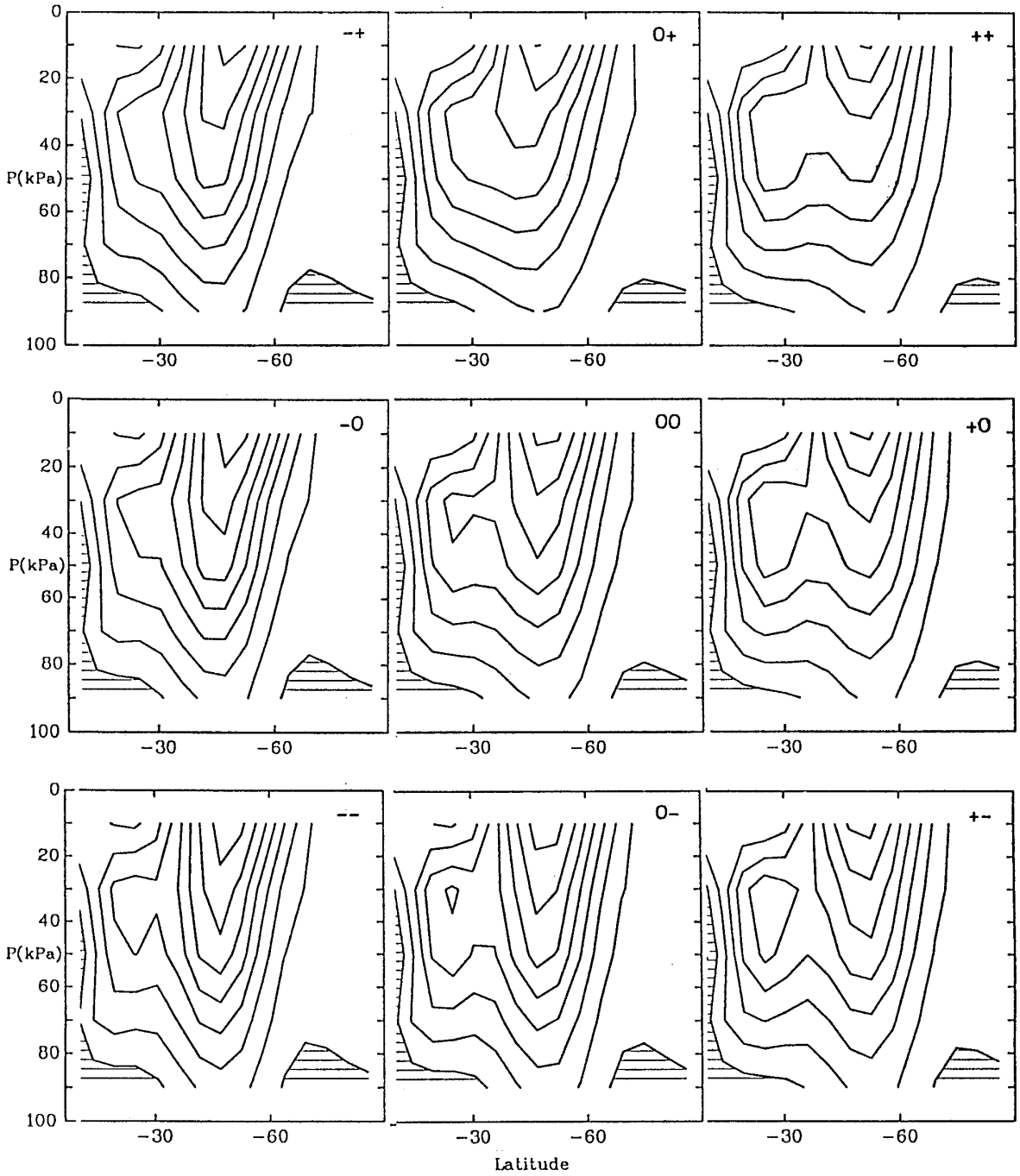

Figure 3. Composite fields of the zonal-mean zonal wind, $[u]$, in the winter hemisphere, illustrating the typical fluctuations of the zonal-mean jets in run A, as determined by the times when EOF1 and/or EOF2 are extremely positive or negative in amplitude. Each field is a composite of the 5% of all days when: EOF1 is most negative (centre left), EOF1 is most positive (centre right), EOF2 is most negative (centre bottom), EOF2 is most positive (centre top). The central picture shows the time-mean case, as in Fig. 1. The fields at the four corners represent combinations of the adjacent fields (see later in text). Contour interval 5 m s^{-1}; easterlies are shaded.

are based on a 200-day sequence near year 51 during which three consecutive propagating anomaly events occurred in the winter mid latitudes. (Note that [KE] is defined as $\frac{1}{2}[(u^*)^2 + (v^*)^2]$, where u^* and v^* denote local deviations of the zonal and meridional winds from the zonal means, $[u]$ and $[v]$, respectively—e.g. locally, $u = [u] + u^*$—and [ ] denotes a zonal averaging operator.)

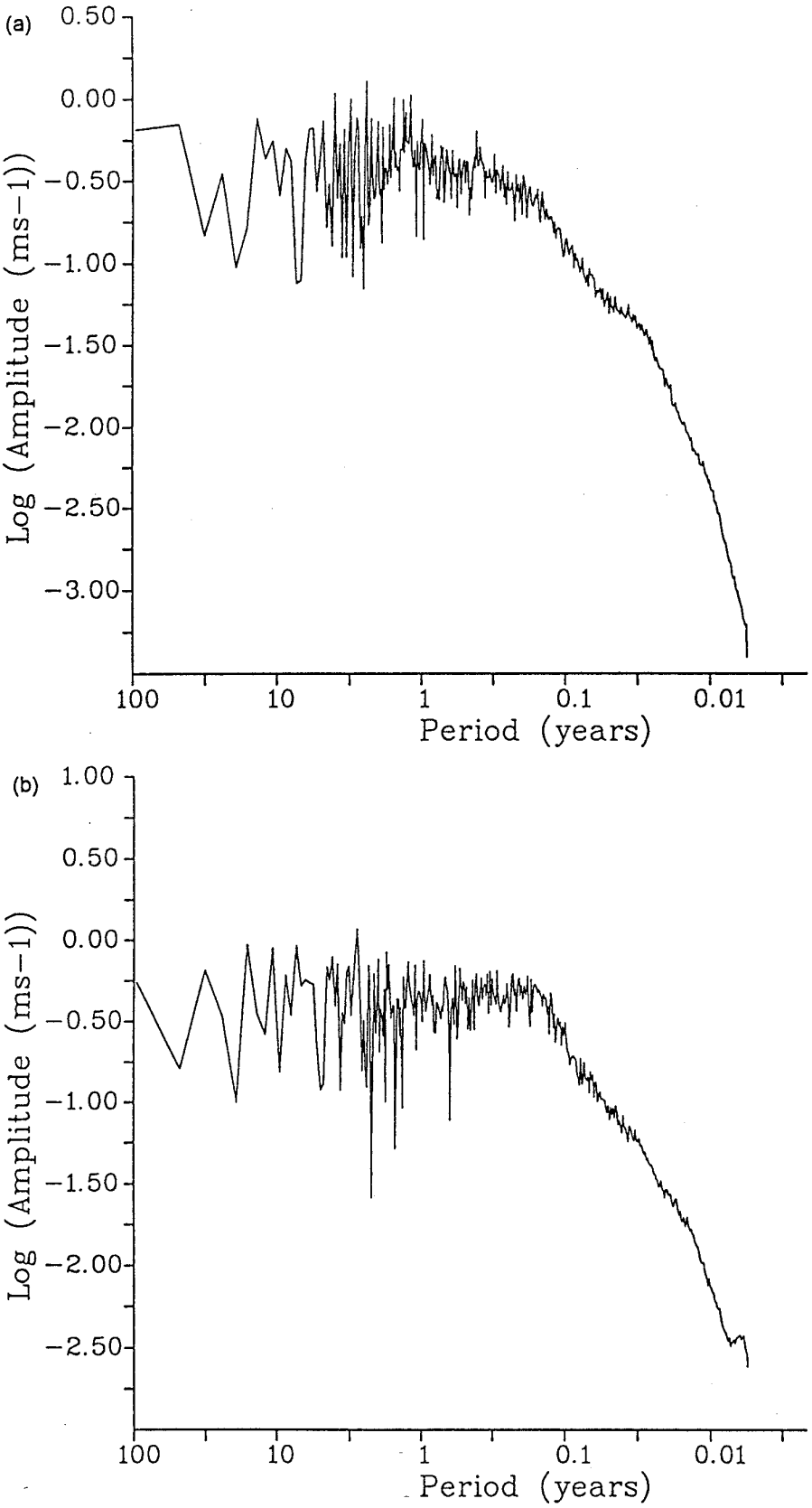

Figure 4. Frequency spectra of PC1 from (a) run A, (b) run B, plotted with logarithmic scales for both amplitude and frequency. Each spectrum has been smoothed by averaging the spectral points into boxes whose size increases logarithmically with frequency. The width of each box in log(frequency) space is, therefore, constant and set somewhat arbitrarily at $120^{-1}\log_{10}(d^{-1})$. Timescales longer than about 1.5 years are effectively unsmoothed.

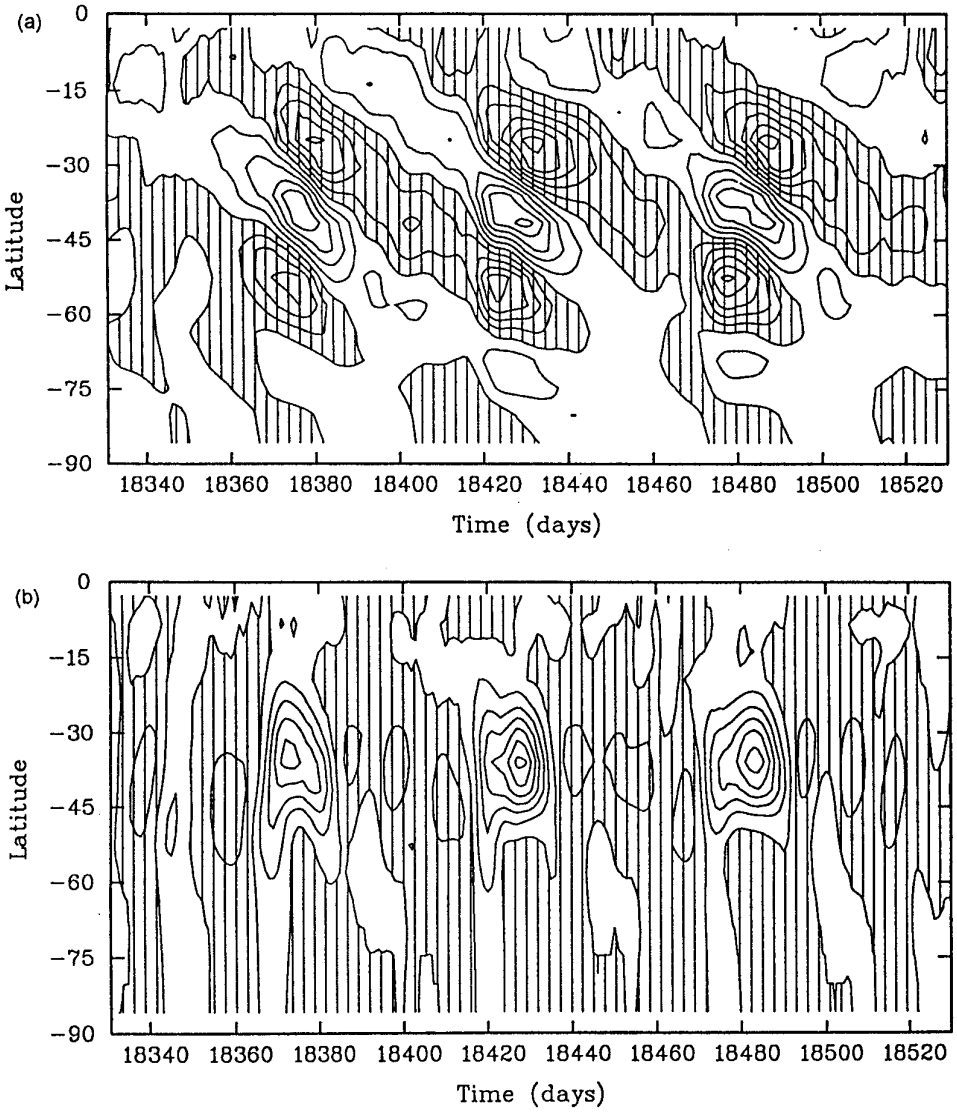

Figure 5. Latitude–time plots of (a) zonal-mean zonal wind, $[u]$ (contour interval 2.5 m s^{-1}; easterly anomalies shaded), (b) zonal-mean eddy kinetic energy, [KE], at 500 kPa in the winter hemisphere (contour interval 25 m^2s^{-2}; negative anomalies shaded). The plots show a 200-day sequence from run B, from day 18 331 to day 18 530 (equivalent to years 50.92 to 51.47). The fields have been passed through a simple 5-day running average and are plotted as anomalies from the respective long-term time means at 50 kPa.

In each event, a tripole of $[u]$ anomalies propagates polewards at a rate of about one degree of latitude per day. The tripole has the same meridional scale as the EOF1 and EOF2 patterns at the mid level. A westerly anomaly is flanked by easterly anomalies and the relationship between the observed tripoles and the EOF patterns is clear. Each tripole pattern grows and decays and its peak amplitude coincides with a positive maximum anomaly of [KE]. Since there is a seven-fold symmetry in longitude, each event must result primarily from the effect of a single synoptic-scale mid-latitude eddy, notwithstanding the presence of smaller-scale (wavenumber-14) components. Hence the spatial characteristics of the anomaly patterns confirm the classical lifecycle picture for the run-B version of the SGCM; although poleward propagation is not part of the classical account.

Eddy growths and the related tripolar anomaly sets do not occur regularly throughout run B, but are a rather intermittent feature. This is demonstrated in Fig. 6 which shows

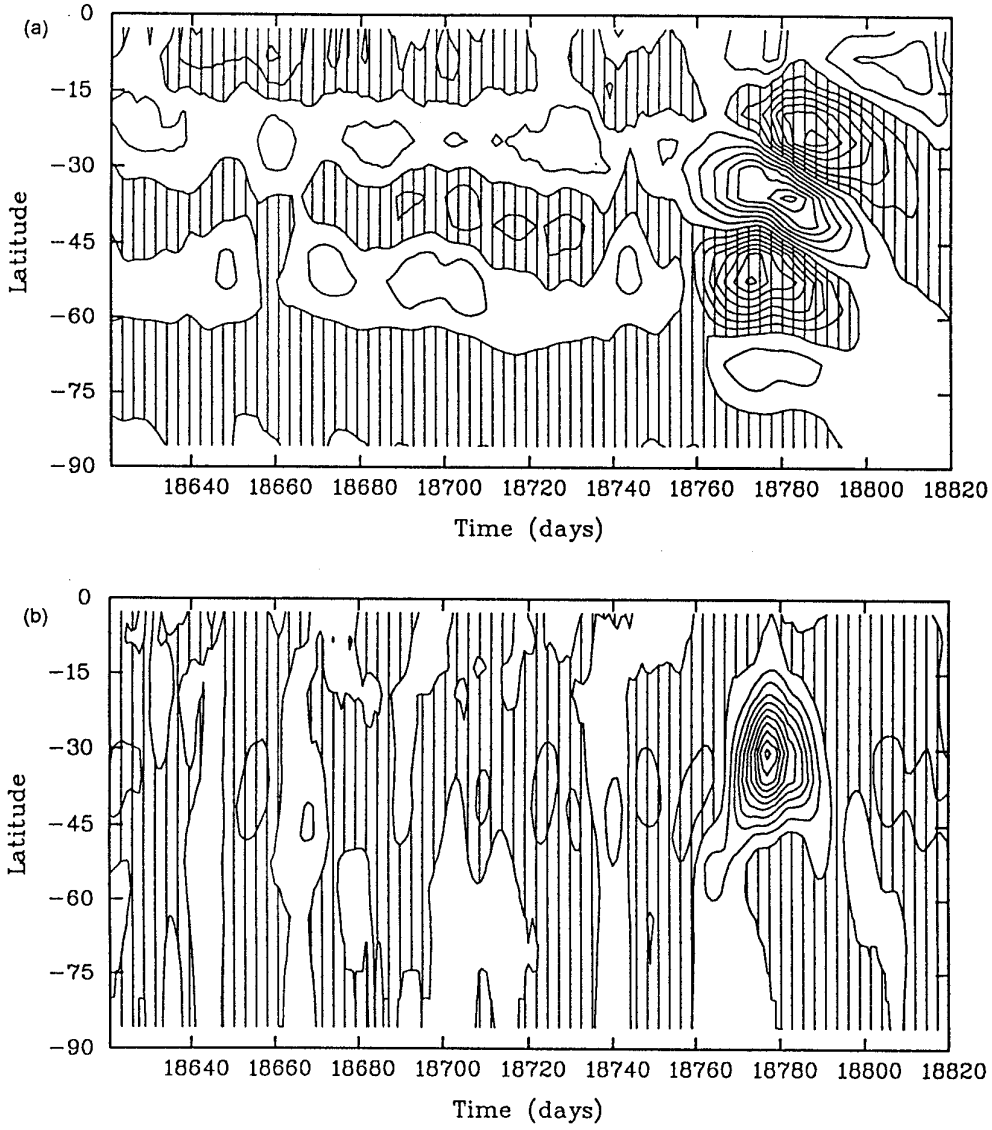

Figure 6. As for Fig. 5, but for the 200-day sequence, days 18 621 to 18 820 (equivalent to years 51.73 to 52.28).

another 200-day sample of the model run, starting 90 days after the end of the sequence in Fig. 5. For nearly 200 days there is little significant eddy activity and a nearly constant weak easterly anomaly between latitudes 30°S and 45°S. Then suddenly a strong wave event occurs, rapidly changing the character of the zonal flow.

(*b*) *The wave–zonal-flow interaction in terms of principal components: a PC-phase space representation*

Since each anomaly pattern propagates polewards, the effects of the wave–zonal-flow interaction can be described compactly in terms of PC1 and PC2, which generally fluctuate in quadrature. Figure 7(a) illustrates this for a 540-day sequence of run B, covering the sequences of Figs. 5 and 6. Each lifecycle corresponds to a sharp dip in PC1, whose time-series is strongly asymmetric about the zero line, and to a sharp positive to negative fluctuation in PC2. The strong lifecycle event is preceded by a long quiescent period lasting some 250 days.

An alternative way of representing the fluctuations of PC1 and PC2 is to plot them as trajectories in a (PC1, PC2) phase-space. Figure 7(b) shows the trajectory of the zonal flow in phase-space over the 540-day sequence of Fig. 7(a). During quiescent periods, the zonal state fluctuates weakly in a region of weakly positive PC1 and near zero PC2. Each lifecycle event takes the zonal state on an anticlockwise loop around the phase-space before returning close to the starting position.

Figure 7(c) confirms that PC1 and PC2 are strongly correlated during strong lifecycle events. Most of the points on the plot come from the quiescent periods. However, the outlying points show a systematic lagged correlation between PC1 and PC2, which reaches a maximum when PC2 leads the negative of PC1 by 11 days. The correlation coefficient in this case is -0.61.

Using the phase-space, we now present a more general description of the form of the wave–mean-flow interaction in the model runs. Figure 8 shows a scatter plot of PC1 against PC2, without lag, for the whole of the last 96 years of run B. The contours indicate the density of points and the vectors represent the time-mean zonal-state trajectories at each phase-space location. The diagram summarizes the long-term time-mean properties of the zonal state. It shows both its static properties in terms of point density and its dynamic properties in terms of the average direction and rate of change of the system as a function of phase-space location. The plot was constructed by dividing the phase-space into 30×30 boxes. For each box, the number of points and the mean trajectory vector between each state-point and the state-point one day later was calculated. Vectors were not plotted for boxes which contained fewer than 3 points in total.

Figure 8 demonstrates a clear anticlockwise circulation. This is associated with the growth and decay of synoptic eddies. That the time-mean trajectories show this unambiguously confirms the dominance of this wave–zonal-flow interaction for the variability in run B. The system spends much of its time in the region of weakly positive PC1. During a strong lifecycle event, however, the trajectories spiral quickly outwards into negative PC1 and move most rapidly during this growth phase. Then as the wave reaches maturity and begins to decay, the trajectories spiral into negative PC2, and finally collapse back into the densely populated quiescent region.

(*c*) *A phase-space circulation timescale*

Considering the direction and magnitude of the time-mean trajectory vectors, it is possible to estimate a circulation timescale, τ_c, as a measure of the average time taken to trace out a circuit of the phase-space. By taking an unweighted average of the tangential velocities of all vectors (unweighted by population density, since we are especially interested in the stronger lifecycle events), τ_c was estimated to be 63 days for run B. To make this estimate, a low-pass Lanczos filter (Duchon 1979) was first applied to the PCs to smooth out the effects of high-frequency fluctuations. An optimal cut-off timescale of 8 days was used, since that yielded a minimum estimate of τ_c.

Error bars can be estimated on the value of τ_c. The standard deviation of individual trajectory vectors about the mean vector in each box is, on average, about 50% of the mean vector magnitude. This, expressed as a variance, is divided by the number of vectors used to compute the mean in each box (about 70 typically) to yield an estimate of the variance of the mean vector length. Since all boxes and their mean vectors are used to estimate τ_c, the variance must be divided further by the effective total number of independent boxes. By estimating a decorrelation time for individual trajectory vector lengths, we find that about 10% of the boxes can be considered as statistically independent. Hence, τ_c is found to be 63 ± 6 days for run B, at the 99% confidence level.

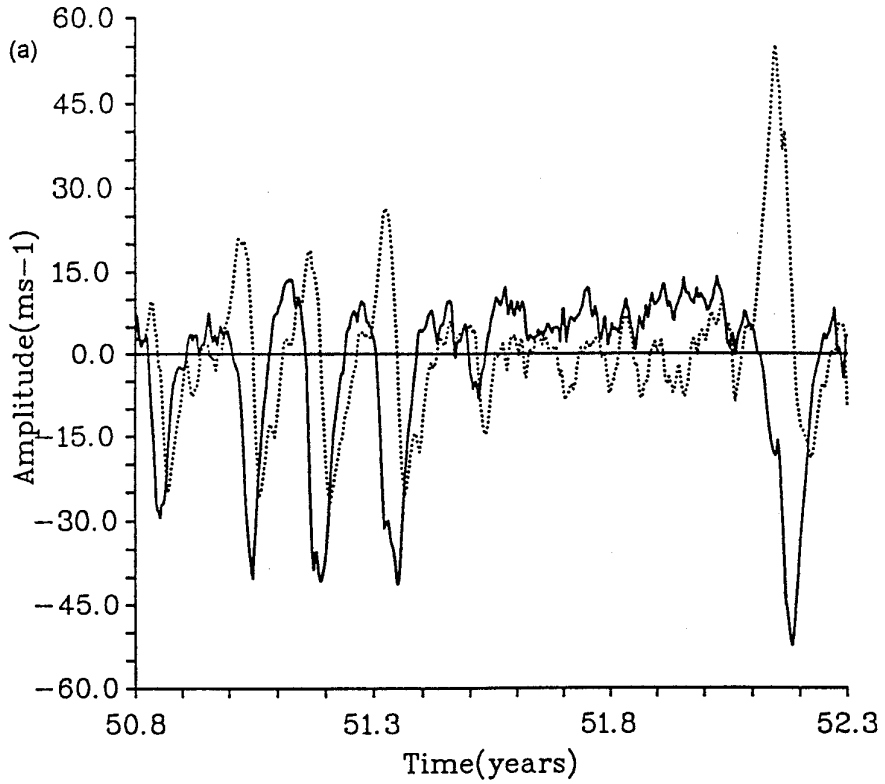

Figure 7. (a) A section of the raw time series of PC1 (thick line) and PC2 (dotted line) from run B, showing days 18 289 to 18 828 (years 50.8 to 52.3). (b) Illustrating the motion of the trajectory vector for the zonal state in PC-phase-space for the same 540-day period of run B as shown in (a). The horizontal x-axis and vertical y-axis are PC1 and PC2, respectively. A small square is plotted on the trajectory every fifth day to indicate phase-space velocities. (c) Scatter plot of PC1, lagged by 11 days, against PC2 for the last 96 years of run B, using daily values. The PC-phase space is divided into 30 by 30 boxes and the contours are of the square root of the number of points per box. Contour interval 3.0. The thick line is the mean value of PC2 as a function of PC1.

This error-bar estimate depends to a first-order of approximation on the assumption that the vectors have a normal distribution about their means.

If low-pass filters are applied with successively longer cut-off timescales, lifecycle events become gradually smoothed out. On interannual timescales, trajectories and population densities for run B look little different from random time-series.

(*d*) *Wave–zonal-flow feedbacks and ULFV*

The estimate of τ_c for run B is close to the timescale where the spectrum of PC1 levels off and that of PC2 peaks. Since it is not possible for lifecycle events to occur simultaneously in the mid latitudes, there is a well-defined energy transfer cycle between synoptic eddies and the zonal flow. Although cycles occur intermittently, there seems to be little scope for ULFV-generating feedbacks between the state of the zonal flow and the growth of disturbances on that flow.

In run A, however, it is quite possible for a number of synoptic-scale waves to develop at different longitudes around a latitude belt. Each of these lifecycles will cause a localized adjustment of the zonal flow which will contribute to fluctuations of the zonal-mean zonal flow and whose effects may, in turn, be advected to the other longitudes by long waves. If, however, the growth and decay of eddies at these other longitudes are in

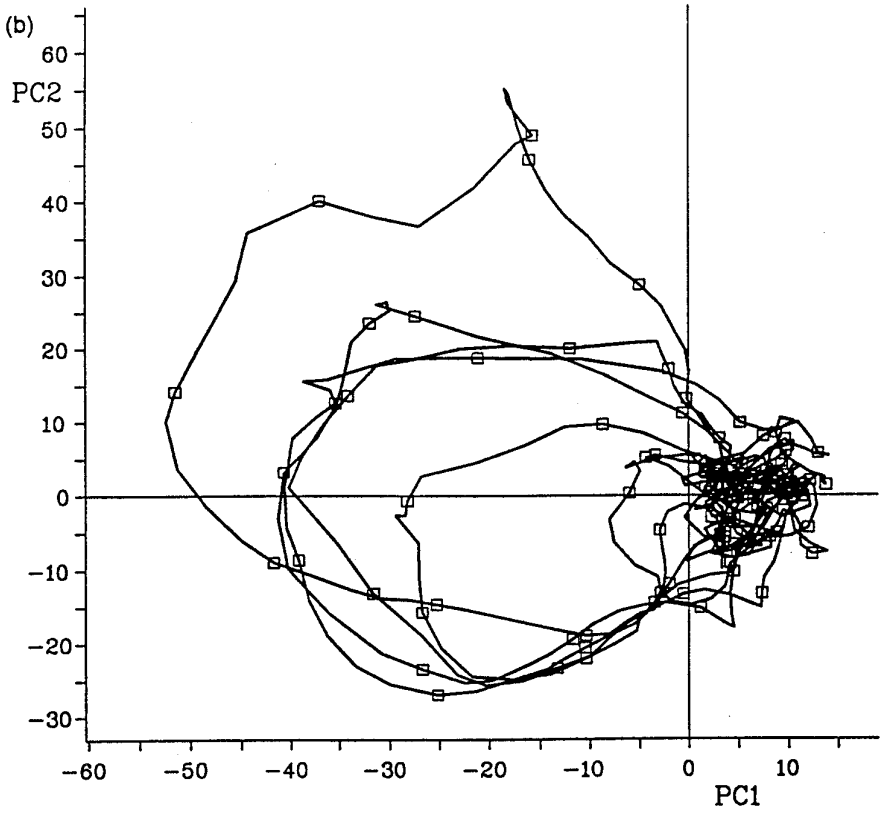

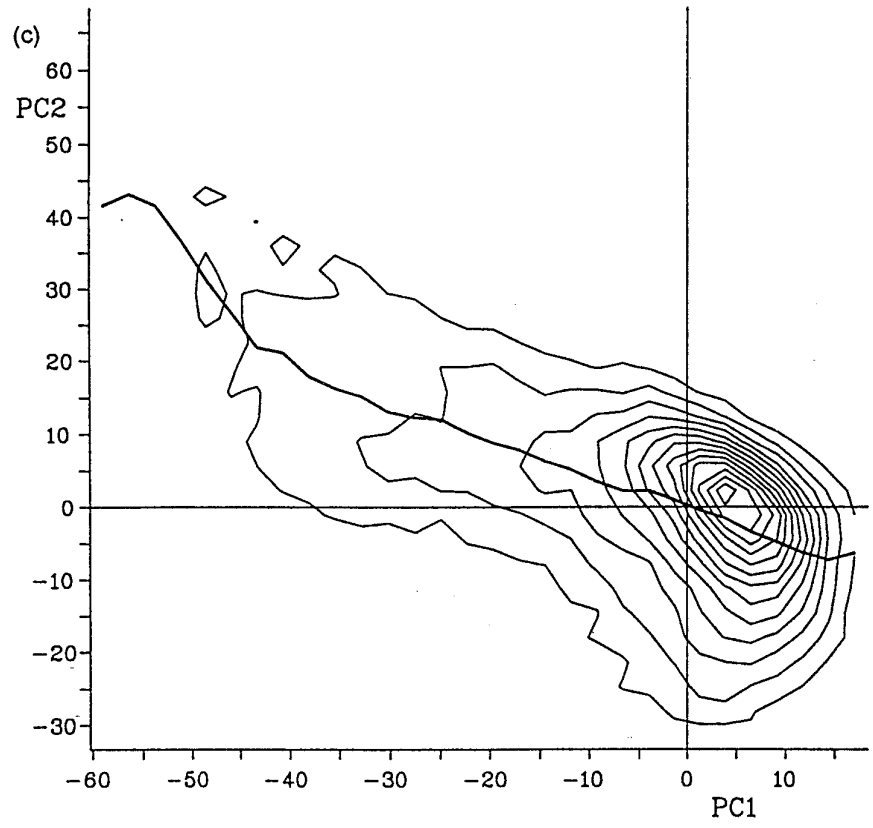

Figure 7. Continued.

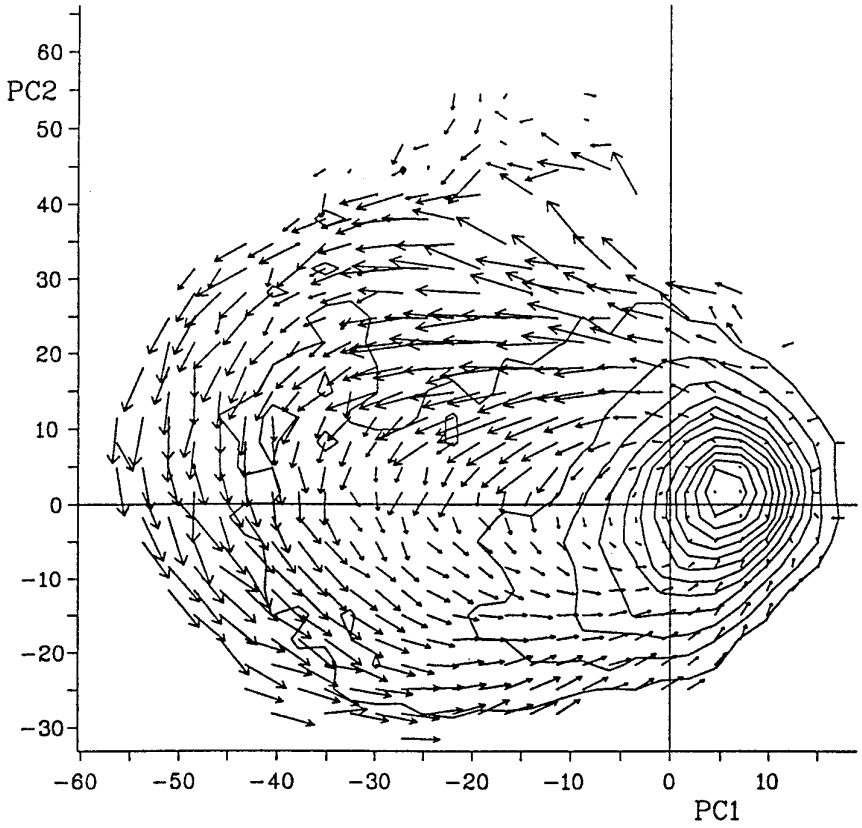

Figure 8. Phase-space plot of PC1 against PC2, low-pass filtered with a cut-off of 8 days, for the last 96 years of run B. Construction of phase-space as in Fig. 7(b). Diagram shows contours of point density as in Fig. 7(c), overlaid with mean trajectory vectors in each box in $m\,s^{-1}\,d^{-1}$. Note that the PC unit is $m\,s^{-1}$.

any way sensitive to the background zonal flow then it is possible to envisage a feedback system emerging.

Our theory regarding a feedback system of this kind is as follows. A lifecycle induces a circuit of a phase-space representing the local zonal flow. This will take the system at least partly round a circuit of the phase-space of the zonal mean as a whole. But since the local effects of the lifecycle will be being continually radiated to other longitudes, the zonal-mean state may not necessarily return to its starting point once the local circuit has been completed. Rather, the adjusting zonal flow may affect the subsequent development of lifecycles elsewhere so as to induce some mean drift of the zonal-mean state in its phase-space.

Figure 9 shows a sample of the raw time-series of the PCs from run A for a 540-day sequence. Neither series, in this case, is asymmetric about zero and eddy-induced peaks are not visually obvious. There is, however, a significant correlation (−0.29) between PC1 and PC2, with PC2 leading PC1 by 11 days. Although this is a lower correlation than in run B, the peak time-lag is identical, suggesting that similar dynamics underlie the PC fluctuations.

If the unfiltered data-sets are used to compute mean trajectory vectors, little circulation is detectable. Instead, vectors on the outer edges of the phase-space point towards the centre. Such a pattern closely resembles that of a random time-series pair, constructed by carrying out a Fourier transformation of the PC time-series, randomizing the phases at all frequencies and then performing an inverse Fourier transformation

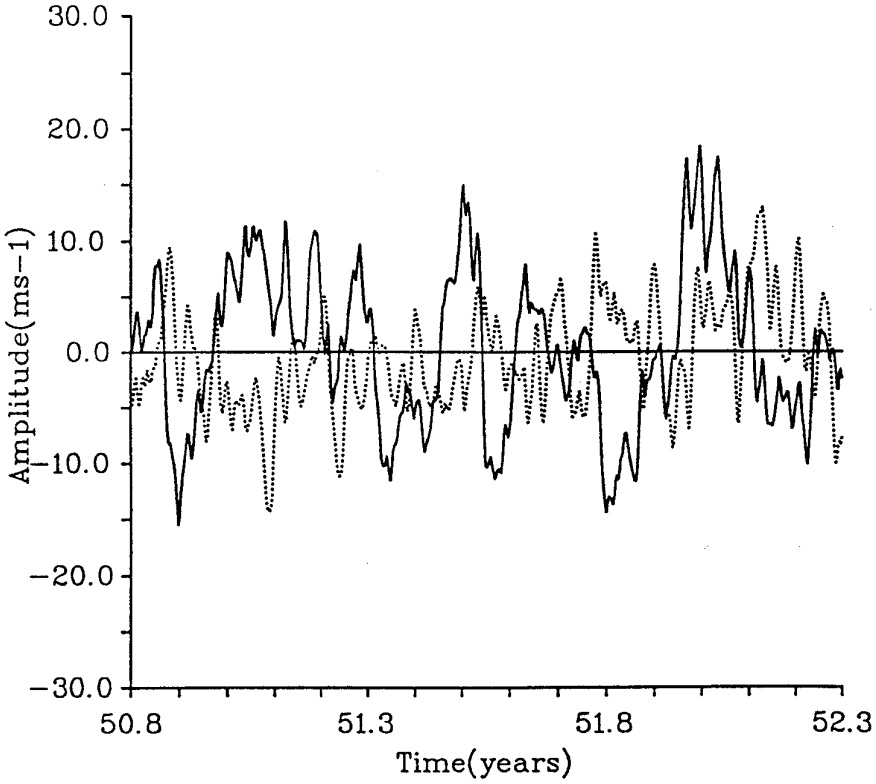

Figure 9. A section of the raw time series of PC1 (thick line) and PC2 (dotted line) from run A, showing days 18 289 to 18 828 (years 50.8 to 52.3).

(hence yielding random data-sets, but with the same spectral power distributions as the originals).

However, if the data-sets are subjected to low-pass filtering, a coherent pattern of mean trajectory vectors emerges. The mean low-frequency drift of the zonal state also takes the form of an anticlockwise circulation. The clearest picture and minimum estimated circulation time occur when a cut-off of 21 days is used in the filter. The associated phase-space diagram is shown in Fig. 10. The vectors form a spiral pointing inwards at an angle of 5 degrees from the tangential direction. The timescale τ_c is estimated to be 152 days and the timescale for the exponential decay of the spiral is approximately 260 days.

The standard deviation of individual vectors about the mean vector in each box is, in this case, about 70% of the mean vector magnitude. Hence, as earlier, we estimate that for run A, τ_c is 152 ± 10 days, at the 99% confidence level. This may be compared with, for example, associated random phase time-series which have no mean circulation, with τ_c typically of the order of 10^4 days in either direction.

Again, when filters with lower frequency cut-offs are used, the vectors gradually lose coherence from the centre of the phase-space outwards, and at interannual timescales are no different from those of random time-series.

The necessity for carrying out low-pass filtering on the data to reveal a mean low-frequency drift in run A is made clear when instead high-pass filtering is used on the data. On timescales shorter than about 20 days, coherent $[u]$-anomaly patterns are seen propagating equatorward, associated with clockwise circulations. Hence, the high-frequency and low-frequency structures largely cancel each other out when the raw data is used. However, we shall not speculate as to what mechanism may be responsible for these high-frequency features.

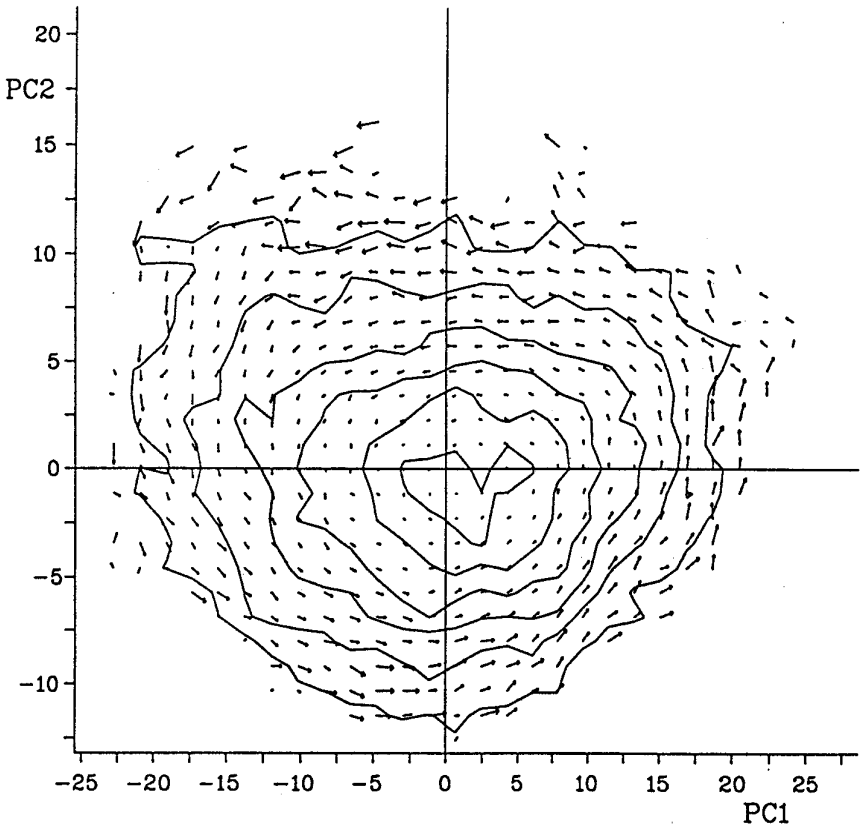

Figure 10. Phase-space plot of PC1 against PC2, low-pass filtered with a cut-off of 21 days, for the last 96 years of run A. Construction of phase-space as in Fig. 7(b). Diagram shows contours of point density as in Fig. 7(c), overlaid with mean trajectory vectors in each box in $m\,s^{-1}\,d^{-1}$.

(*e*) *Band-pass filtering*

Band-pass filters, with appropriately chosen cut-offs to isolate timescales typical of the run-B lifecycles, have been applied to the run-A time-series. These show whether or not the low-frequency drift in run A results from interacting lifecycles of the type seen in run B.

Several of these filters were first tested on run B to find an optimum cut-off range. The results were found not to be sensitive to the precise cut-off values. For direct comparison, phase-space diagrams for runs A and B in which a 40-to-60-day band-pass filter was used are shown in Fig. 11. (Note that the value of τ_c for run B of about 63 days includes slow-moving trajectories in the quiescent region, so trajectories within lifecycle events are well captured by this filter.) In run B, the filter results in giving a more circular form to the mean trajectory pattern and, despite the differences between the models, the pattern is remarkably similar to that of run A. The circulation in run A is about 30% weaker compared to run B, and the spatial scale is smaller, but this is to be expected in view of the complications introduced by long waves and multiple lifecycles in the former case.

(*f*) *The relationship to frequency spectra and ULFV*

The results above suggest that the low-frequency fluctuations of the zonal flow in run A are associated with multiple lifecycle events, similar to those seen in run B. However, these findings alone are not sufficient to prove that the low-frequency drift

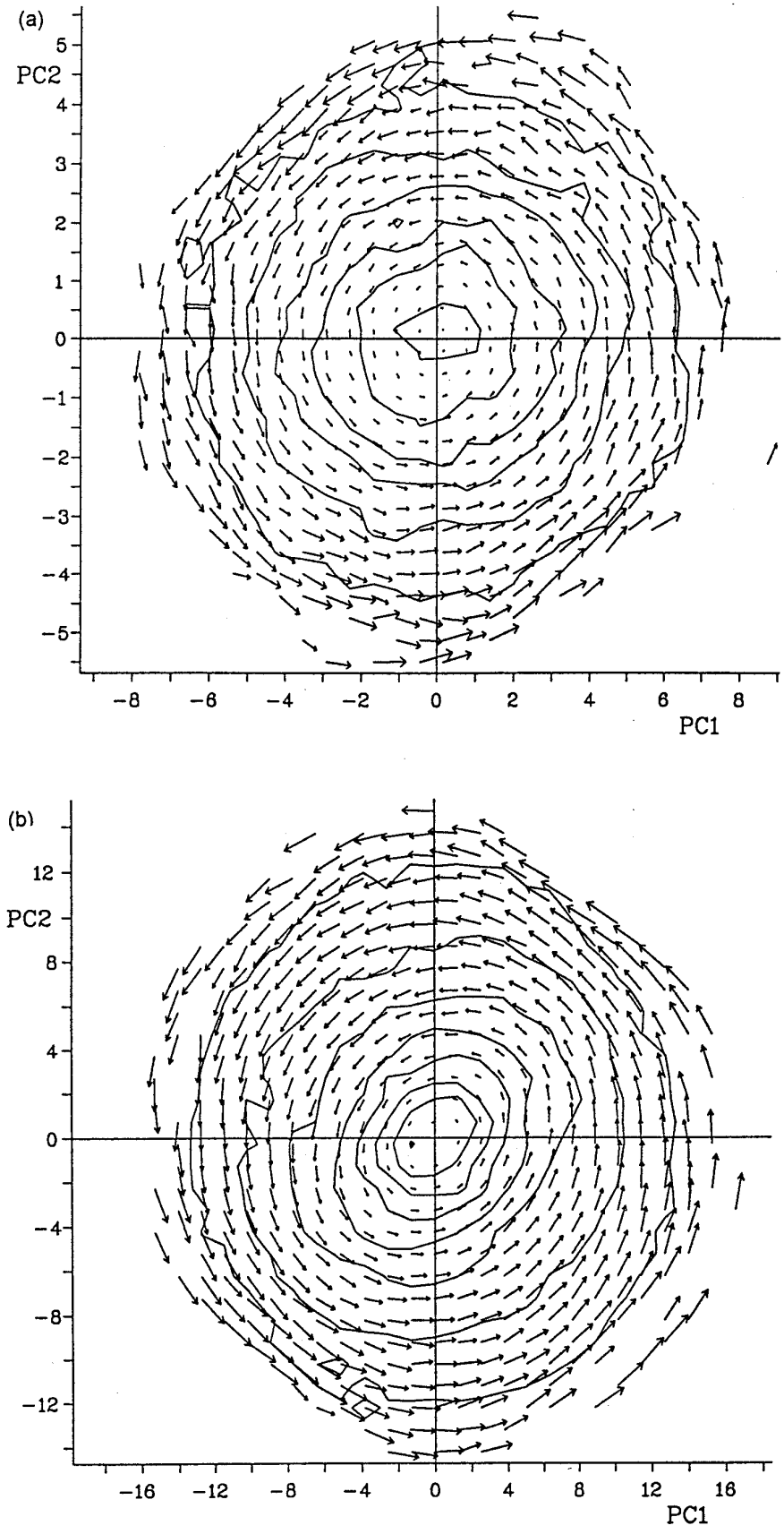

Figure 11. Phase-space plots of PC1 against PC2, band-pass filtered with cut-offs at 40 days and 60 days, respectively, for the last 96 years of (a) run A, (b) run B. Construction of phase-space as in Fig. 7(b). Diagram shows contours of point density as in Fig. 7(c), overlaid with mean trajectory vectors in each box in $m\,s^{-1}\,d^{-1}$.

results specifically from interactions associated with multiple lifecycles. Rather it may simply be a result of the remnants of many lifecycle–timescale circulations superimposed on each other and with lower frequency (and possibly more random) fluctuations. So the net effect is to produce, statistically, a low-frequency circulation, with a timescale somewhat longer than that of individual lifecycles.

Nevertheless, it is clear that coherent, very-low-frequency structures do appear in the ensemble statistics of run A, and that multiple lifecycles are the root cause of this. The most important point, then, is one of timescale. In run A, the mean low-frequency circulation has a timescale of some 150 days, which is therefore an internally generated intrinsic timescale of the fluctuations of the zonal-mean zonal jets, yet it is much longer than either the typical timescale of synoptic-scale waves or the longest explicitly forced timescale of 30 days (τ_E).

The zonal state of run A fluctuates quite wildly across the phase-space on timescales often much shorter than τ_c. However, the existence of a background circulation enhances the very-low-frequency components of the variability, via long-timescale ensemble statistics. Since τ_c is only an average measure of a feature which may be highly variable, the resulting spectral peaks are considerably broadened, possibly extending into the ULFV range as in the spectrum of PC1 in Fig. 4.

In summary, it is suggested that multiple wave–zonal-flow interactions, which lead to the observed mean phase-space circulation, may be at the root of ULFV in the zonal jets.

4. Linear normal modes and lifecycle experiments

The nature of wave–zonal-flow interactions in the SGCM have been described only quantitatively so far. In this section, we show how the dynamics of multiple lifecycle events may lead to the particular zonal adjustments that have been described. We shall examine the growth and decay of baroclinic waves on various zonal flows, corresponding to different locations in phase-space.

(*a*) *Setting up the initial zonal mean states*

Zonal-mean states corresponding to large negative and positive amplitudes of the EOF1 pattern were constructed by JJ92. The fastest growing linear normal modes on each of these states was integrated through a nonlinear lifecycle. These experiments provided some evidence for positive feedbacks between eddies and the mean flow. However, the calculation was limited in scope on two counts. First, JJ92 did not consider the effect of EOF2 on the character of the problem, yet it has now been shown that both EOFs need to be considered together. Secondly, JJ92 ignored the effects of friction and heating on the baroclinic lifecycles. Newtonian cooling and Rayleigh friction have a substantial impact on baroclinic lifecycles. Both these terms act directly to inhibit the growth of unstable eddies. The Rayleigh friction also acts to reduce the horizontally sheared barotropic correction to the wind which builds up during the nonlinear phase of the lifecycle and which is the major factor in the saturation of the baroclinic eddies in the Simmons and Hoskins (1978) lifecycles (James 1987). The net effect of the dissipative terms is unpredictable but large; their inclusion requires some modifications of the model, to be discussed shortly.

Composite zonal-mean states for nine distinct regions of the phase-space were produced. For each composite, the values of PC1 and PC2 are examined on each day of run A, and all cases in which a certain criterion is exceeded are taken, with the criterion set so that each composite uses 5% of the total data-set. These criteria give composites

for the most positive and most negative 5% of cases of both PC1 and PC2 (the ends of the horizontal and vertical axes of the phase-space) and similarly along the diagonal axes (by re-mapping PC1 and PC2 onto axes at 45 degrees to the original). This then gives eight balanced zonal-mean states which represent the range of variations through the course of the run. In the paper by JJ92, the composite states used 10% of the available data. In this paper, the states become more widely separated on this two-dimensional space by taking 5% composites. The ninth state is simply the time-mean state, in the centre of the phase-space.

The winter hemisphere $[u]$-fields of the nine composites were shown in Fig. 3. The states along the horizontal and vertical axes will be referred to as $-\bigcirc$, $+\bigcirc$; $\bigcirc-$,$\bigcirc+$, respectively, and the time-mean state as state $\bigcirc\bigcirc$. Similarly, the composites along the diagonal axes will be referred to as states $--$, $-+$, $+-$ and $++$. Hence, in this notation, the first symbol refers to the phase of EOF1, and the second to the phase of EOF2, for each composite.

(*b*) *Linear normal-mode calculations*

For each of the nine states, the fastest growing mid-latitude winter-hemisphere wavenumber-7 linear normal mode has been computed, with the dissipative parametrizations in place. Wavenumber-7 was chosen since it was found to have the fastest growth rates relative to other wavenumbers. The growth rate of each mode, computed using an eigenvalue method (Wyatt 1981), is given in Table 1, together with the corresponding growth rates under frictionless, adiabatic conditions.

TABLE 1. GROWTH RATES OF THE DISSIPATIVE LINEAR NORMAL MODES

Zonal state	Growth rate (d^{-1})
$\bigcirc\bigcirc$	0.179 (0.404)
$-\bigcirc$	0.199 (0.438)
$+\bigcirc$	0.122 (0.333)
$\bigcirc-$	0.189 (0.411)
$\bigcirc+$	0.143 (0.394)
$--$	0.205 (0.434)
$-+$	0.184 (0.430)
$+-$	0.150 (0.368)
$++$	0.111 (0.321)

The growth rates for a frictionless, adiabatic atmosphere are given alongside in parentheses.

There are substantial differences in growth rates between the various states, with the largest variations along the EOF1 axis and along the diagonal from state $--$ to state $++$, where the growth rate varies by a factor of 1.85. Dissipation reduces the growth rates of the modes in all cases, by factors of 2 to 3 compared to the dissipationless cases, in good agreement with the findings of Valdes and Hoskins (1988).

(*c*) *Lifecycle integrations of normal-mode perturbations*

The SGCM was integrated for the equivalent of 50 days to generate a nonlinear baroclinic lifecycle, with each zonal-mean state as the initial state and the linear normal mode as an initial disturbance, scaled to have a maximum surface pressure perturbation of 0.1 kPa.

In the presence of heating, friction and the mean meridional circulation, zonal-mean states based on the time-average climatology or on composites from run A are not stationary states of the governing equations. Consider, by way of example, the climatological mean state for which the balances operating in the system can be expressed in the form

$$\frac{\partial \mathbf{X}}{\partial t} = \overline{\mathbf{T}}_m + \overline{\mathbf{T}}_e + \frac{\mathbf{X}_E - \overline{\mathbf{X}}}{\tau_E} = 0 \tag{1}$$

where $\mathbf{X}$ represents the dynamical state of the system, $\mathbf{X}_E$ the equilibrium state of the system and $\overline{\mathbf{X}}$ its climatological mean. $\mathbf{T}_m$ are tendencies associated with the mean meridional circulation, $\mathbf{T}_e$ the tendencies associated with the eddy fluxes, and the last term represents heating and friction. If a zonal-mean state based on the climatology is used to initialize the model, then

$$\frac{\partial \mathbf{X}}{\partial t} = \overline{\mathbf{F}} = \overline{\mathbf{T}}_m + \frac{\mathbf{X}_E - \overline{\mathbf{X}}}{\tau_E} \tag{2}$$

In order that the state $\overline{\mathbf{X}}$ should be a stationary state of the system, the governing equations must be modified so that

$$\frac{\partial \mathbf{X}}{\partial t} = \overline{\mathbf{T}}_m + \overline{\mathbf{T}}_e + \frac{\mathbf{X}_E - \overline{\mathbf{X}}}{\tau_E} - \overline{\mathbf{F}} \tag{3}$$

The vector $\overline{\mathbf{F}}$ was generated by calculating the tendencies associated with the climatological zonal-mean state with no eddies, i.e. from Eq. (2). The same technique can be applied when $\overline{\mathbf{X}}$ represents some composite zonal-mean state.

Figure 12 shows the vertically integrated eddy kinetic energy as a function of time for the lifecycles on the five zonal states along the main PC1 and PC2 axes. The modes grow to peak amplitudes that are smaller than those of the dissipationless cases of JJ92; they also have a much slower decay phase.

In conjunction with the differences in growth rates, the mode on state −○ grows to a peak amplitude of about 18 kJ m^{-2}, while the mode on state +○ grows to a much weaker amplitude of only 5 kJ m^{-2}. The peak amplitudes reached by the ○− and ○+

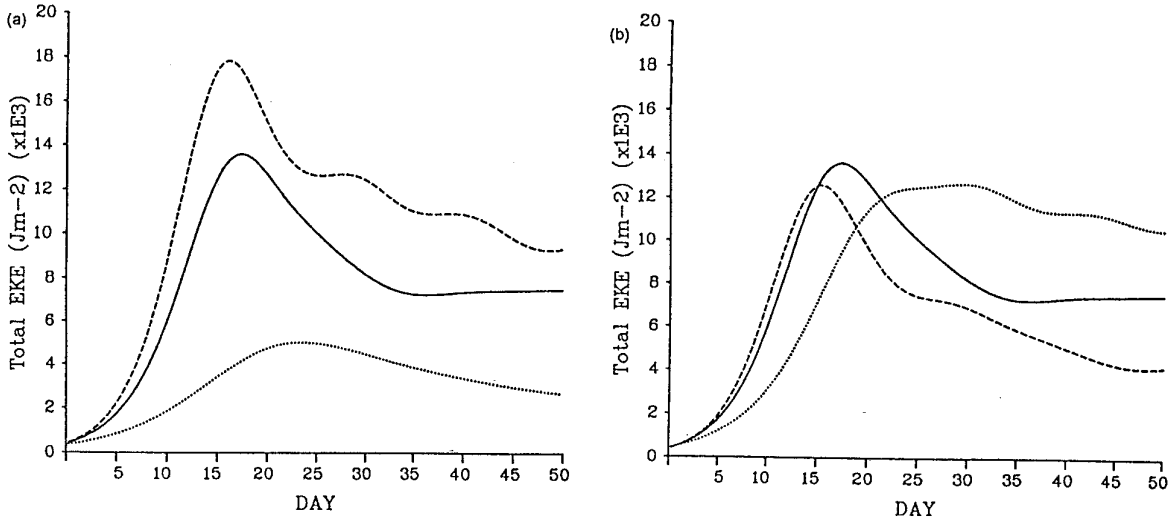

Figure 12. Graphs of total eddy kinetic energy, [KE], against time through the course of the lifecycles of the normal-mode perturbations. Zonal states used: (a) ---- State −○, —— State ○○, ... State +○; (b) ---- State ○−, —— State ○○, ... State ○+.

modes are similar to each other and to the ○○ mode, although the ○+ mode, which starts with a smaller growth rate, takes some 15 days longer than the ○− mode to achieve the peak, and subsequently has a very slow decay phase. The lifecycles are clearly sensitive to the values of PC1 and PC2. The inclusion of surface drag and Newtonian cooling accentuates the differences across the EOF1 axis compared to the frictionless, adiabatic results of JJ92.

From a comparison of Fig. 12 with Fig. 5(b), it is clear that the normal-mode perturbations grow very weakly in comparison with the eddies observed during run B itself; their peak amplitudes differ typically by an order of magnitude. This suggests that the growth of eddies from small-amplitude, normal-mode structures may not be the most efficient mechanism for the conversion of available potential energy to eddy kinetic energy. Rather, eddy kinetic energy in the long runs of the SGCM often results from the interaction and locking together of finite-amplitude upper-level and low-level disturbances with favourable phase relationships, in the manner discussed by Farrel (1985).

Nevertheless, there is evidence that zonal flow interactions involving normal modes and those involving model-run eddies do share some similar properties in relation to the PC-phase space, in spite of the small amplitudes of the former.

(*d*) *Phase-space composites of model eddy kinetic energy anomalies*

Figure 13 shows winter hemisphere composite fields from run A of eddy kinetic energy anomalies. The composites correspond to the eight extreme states of zonal wind discussed in section 4(a). These composites vary systematically with the zonal flow state. Negative anomalies are more prevalent for states −−, −○, −+ and ○+, while positive anomalies dominate for states ++, +○ and +−. The largest differences span the EOF1 axis. In the −○ state, an intense positive anomaly of 22 $m^2 s^{-2}$ is centred near latitude 40°S, while in the +○ state a negative anomaly of 10 $m^2 s^{-2}$ is seen in a similar location.

The growth rates and peak eddy kinetic energy in the lifecycle experiments depend in a similar way on the zonal-flow state. The eddies growing from normal modes grow more vigorously when the zonal state corresponds to negative EOF1. At the same time, a finite-amplitude eddy lifecycle in the model run induces a circulation of the mean flow in phase-space, as shown in Fig. 8. The associated [KE] is largest during the leftmost section of the circuit (negative PC1), as can be seen from Fig. 5(b). Run A consists of a succession of lifecycles which interact with the zonal flow to induce a background, lower-frequency circulation. Thus, on average, there will be a greater proportion of leftmost sections of circuits nearer to the left-hand side of phase-space than on the right-hand side, so leading to the observed bias in [KE] anomalies.

(*e*) *The effect of the normal-mode lifecycles on the zonal flow*

The zonal-mean flow is modified by the lifecycle of a normal-mode perturbation. Figure 14 illustrates the change of $[u]$ between the start of a typical lifecycle and day 30, after the perturbation has reached maturity and is beginning to decay.

A tripole of $[u]$ anomalies has developed in the mid-latitude flow. An easterly anomaly, with a peak amplitude of about 3 $m s^{-1}$, is centred in the upper troposphere near latitude 38°S. It is flanked by westerly anomalies centred near latitudes 18°S and 58°S. The latter, more poleward, anomaly is weak and has an associated low-level anomaly centre near latitude 51°S.

These adjustments to $[u]$ have a similar structure to the EOFs in run A, shown in Fig. 2, although the meridional scale is slightly larger. The amplitude of the $[u]$ anomaly is equivalent to a PC anomaly of about 7 $m s^{-1}$ when mapped onto the EOF patterns.

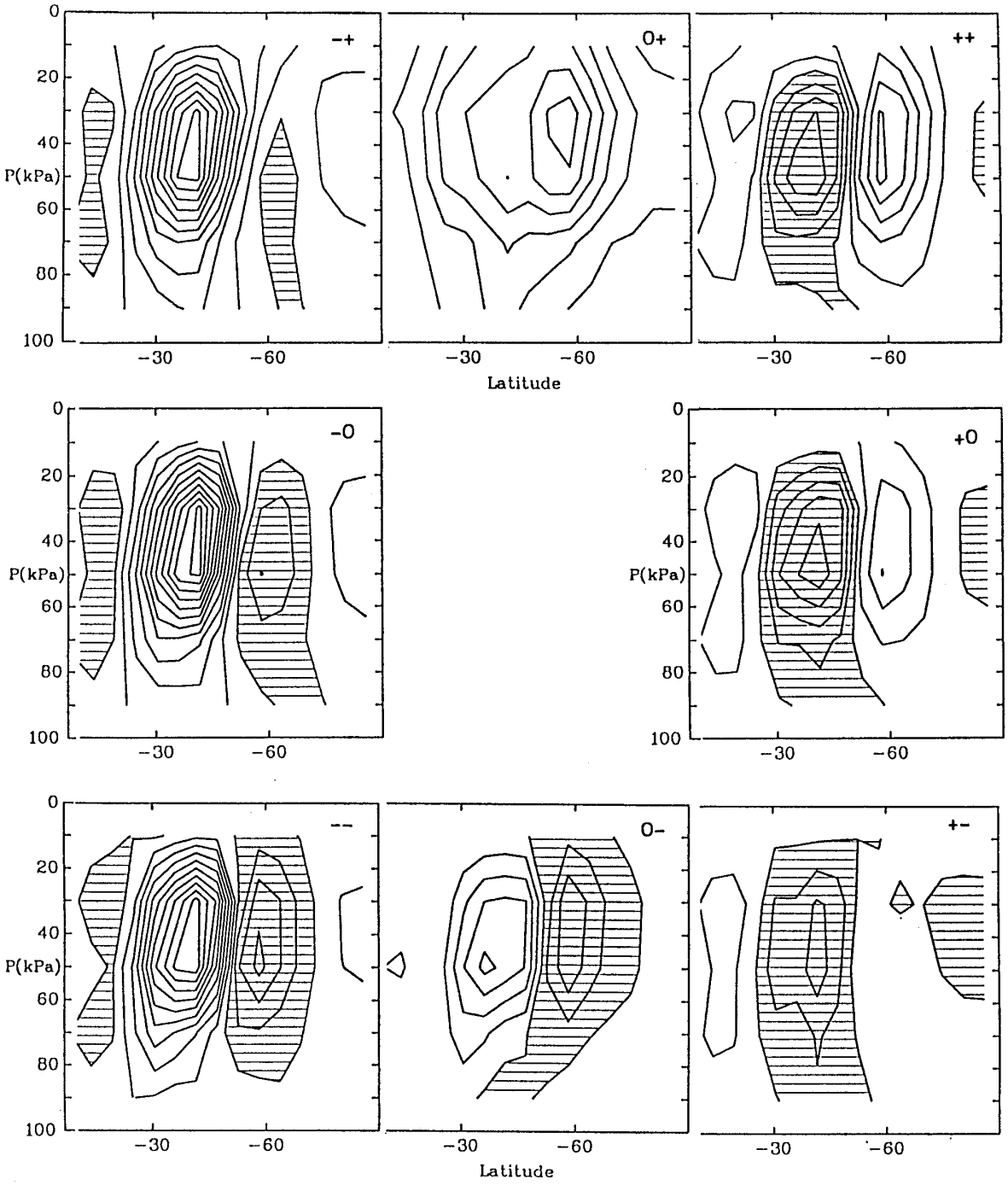

Figure 13. Composite fields of zonal-mean eddy kinetic energy, [KE], in the winter hemisphere, as anomalies from the time mean, for run A. The fields are constructed using the same procedure, based on the amplitudes of PC1 and PC2 of $[u]$, as used to compute the zonal states shown in Fig. 3 and correspond spatially to these states on the PC-phase space. Contour interval is 2 $m^2 s^{-2}$, anomalies below -1 $m^2 s^{-2}$ are shaded.

Such amplitudes are typical of the short-term fluctuations of the PCs in run A, but are typically only around 20% of the magnitude of the lifecycle circuits of run B.

The $[u]$-fields during each of the nine lifecycle integrations are now mapped onto EOFs 1 and 2 of run A. The equivalent modifications to PC1 and PC2 are plotted in Fig. 15 on the phase-space as trajectories showing the zonal state changes during each experiment.

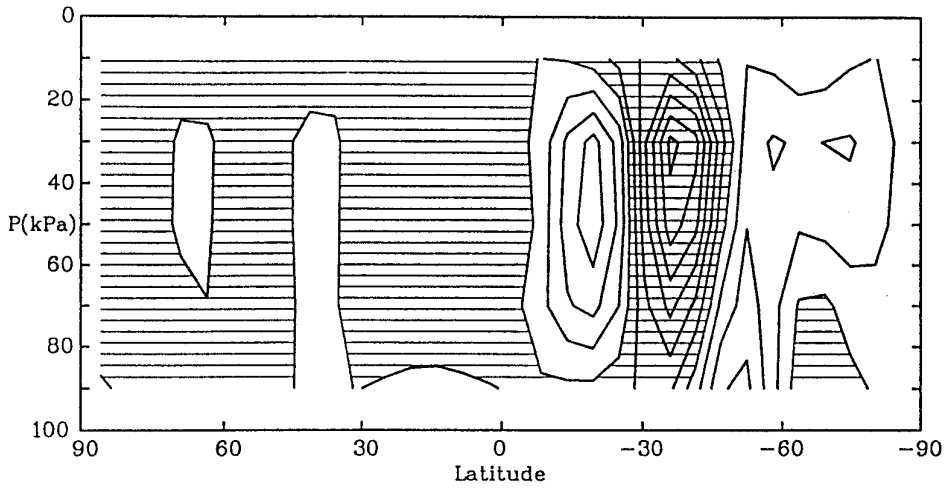

Figure 14. The change induced in the $[u]$-field due to a normal-mode perturbation lifecycle using the $-\bigcirc$ zonal-mean field as the initial state, from the start of the integration to day 30. Contour interval 0.5 m s^{-1}; easterly anomalies are shaded.

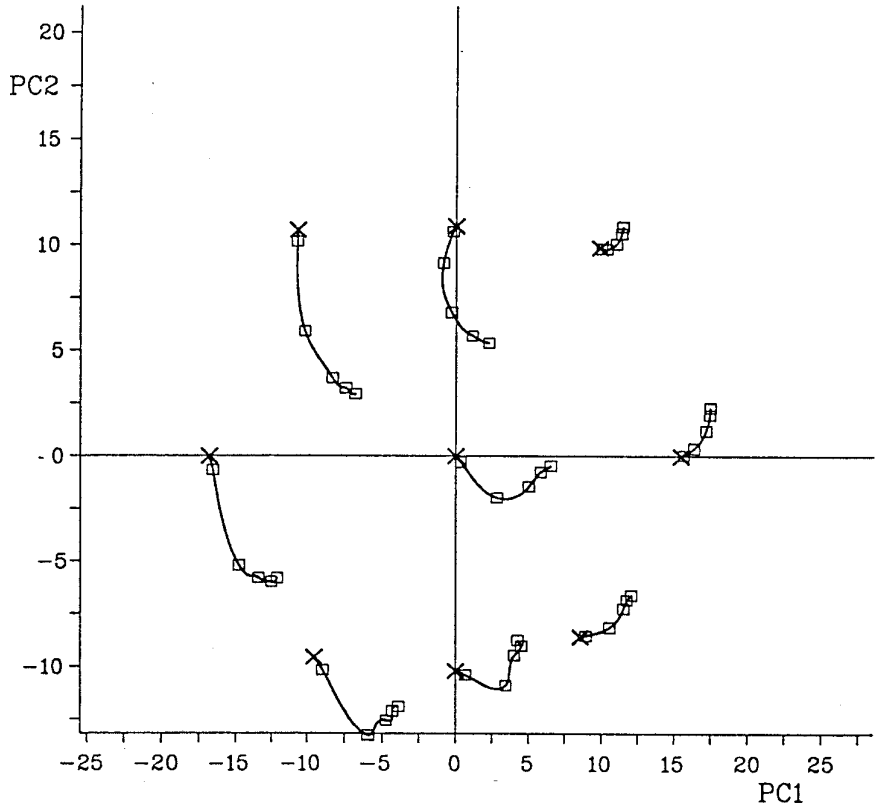

Figure 15. PC-phase-space plot showing the total change in $[u]$, as indicated by the values of PC1 and PC2, due to the growing and decaying normal-mode perturbation. For each of the nine initial zonal states used, a trajectory is plotted showing the induced changes from the start of the lifecycle experiment until day 50. A cross is plotted at the starting position of each experiment. Subsequently, squares are plotted to indicate the position of the respective states every tenth day (i.e. at days 10, 20, 30, 40 and 50). The scale of the axes are identical to those of Fig. 10, for comparison.

The lifecycle events push the zonal state in a generally anticlockwise trajectory in the phase-space, somewhat similar to the circulations of runs A and B. Thus, wherever its starting position is, the zonal state will be taken a little further along a general circuit by a lifecycle. However, the circulations induced by model eddies and by lifecycles of normal-mode perturbations do have some dissimilarities. In the O+ sector, the perturbation lifecycle trajectories are nearly at right angles to those of the model data. Furthermore, there is a substantial drift away from the centre of the phase-space.

Connecting these points, the anticlockwise circulation generated by the perturbation lifecycles is centred not on the middle of the phase-space, but on some location in the ++ quadrant. In the absence of other influences, the zonal state would drift slowly into this quadrant with the weak modes there unable to induce a jump towards more negative EOF1 so that a new circuit could begin. An escape from the ++ quadrant could be facilitated by other interactions, for example involving long waves.

In summary, growing normal-mode perturbations interact with the zonal flow to induce low-frequency, anticlockwise phase-space trajectories. The underlying mechanism is not perhaps the same as that for the model eddy circulation of run A, which specified multiple lifecycle interactions. The flow in the SGCM may indeed be governed by elements of both normal-mode-type growths and finite-amplitude disturbances, despite the latter being dominant. Certainly, both descriptions have been shown to possess broadly similar properties.

5. Conclusions

In extending the work of JJ92, we have investigated wave–zonal-flow interaction in the SGCM, testing the theory that it contains an implicit feedback system leading to internally generated ULFV.

Run B, integrated with an imposed seven-fold symmetry in the zonal direction, allowed a study to be made of interactions involving successions of single synoptic-scale-wave lifecycles. Each lifecycle took the zonal-mean state on an anticlockwise circuit of phase-space, beginning and ending in a similar region of the space. Since the simultaneous occurrence of lifecycle events was not possible in run B, there was little net effect between start and finish of an event and little possibility of feedback.

However, in run A, in which both long waves and simultaneous synoptic developments at different longitudes were possible, the adjusting zonal state during one lifecycle event interacts with subsequent events inducing a background, mean, low-frequency phase-space circulation, on a timescale of about 150 days. This timescale, τ_c, is intrinsic to the internal dynamics of the model. It is much longer than the timescale of the transient, synoptic-scale eddies that drive it and results in very-long-timescale oscillations of the zonal flow, which extend to the ULFV range. We suggest that this alone may account for much of the ULFV observed in the simple model.

The possibility of a normal-mode description of the wave–zonal-flow interactions has also been investigated. Dissipative linear normal modes were calculated and allowed to grow through nonlinear lifecycles on different zonal states across the phase space. The growths were surprisingly weak in comparison with those occurring in the SGCM runs, but also induced broadly anticlockwise phase-space trajectories.

A normal-mode description alone cannot account for the strength of eddy growths in the model runs. An appeal to finite-amplitude concepts also needs to be made. Admittedly, neither description has, individually, the necessary characteristics to prove that an explicit feedback system exists in relation to wave–zonal-flow interaction. Taken

together, however, the discoveries of eddy amplitude biases and low-frequency circulations in phase-space may yet yield further insights in this area.

We have demonstrated that wave–zonal-flow interaction sets up an intrinsic long timescale and may be implicit in the generation of ULFV. We have not attempted to fit a complete model of the underlying dynamical causes. This must undoubtedly be attempted in due course. Future work is also intended to study wave–zonal-flow interactions in more sophisticated GCMs, such as in the 10-year integrations of ECMWF-based models being carried out at Reading, and in observational data-sets. The possibility that the findings described here for the SGCMs may apply more widely could have important consequences for the study of internal atmospheric low-frequency variability in general.

Acknowledgements

The authors thank the UK Universities' Global Atmospheric Modelling Programme for making computer resources at the Rutherford Appleton Laboratory available to perform the model integrations, and to the respective computer centres at the University of Reading and at the Freie Universität, Berlin for the use of further computing facilities. PMJ is grateful for the support of a NERC fellowship during the period of this research and for the additional support of a BMFT grant, KFT 306, which enabled PMJ to conduct part of this work at the Freie Universität, Berlin. PMJ also thanks Chris Larnder of the McGill University in Montreal for providing the logarithmic smoothing algorithm used on the frequency spectra.

References

Duchon, C. E. 1979 Lanczos filtering in one and two dimensions. *J. Appl. Meteorol.*, **18,** 1016–1022

Farrel, B. F. 1985 Transient growth of damped baroclinic waves. *J. Atmos. Sci.*, **42,** 2718–2727

Hoskins, B. J., Hsu, H. H., James, I. N., Masutani, M., Sardesmukh, P. D. and White, G. H. 1989 'Diagnostics of the global circulation based on ECMWF analyses 1979–1989'. *World Climate Research Programme* 27, WMO/TD No. 326

James, I. N. 1987 Suppression of baroclinic instability in horizontally sheared flows. *J. Atmos. Sci.*, **44,** 3710–3720

James, I. N. and Gray, L. J. 1986 Concerning the effect of surface drag on the circulation of a baroclinic planetary atmosphere. *Q. J. R. Meteorol. Soc.*, **112,** 1231–1250

James, I. N. and James, P. M. 1989 Ultra-low frequency variability in a simple atmospheric circulation model. *Nature*, **342,** 53–55

1992 Spatial structure of ultra-low-frequency variability of the flow in a simple atmospheric circulation model. *Q. J. R. Meteorol. Soc.*, **118,** 1211–1233

Kidson, J. W. 1988 Indices of the southern hemisphere zonal wind. *J. Clim.*, **1,** 183–194

Lorenz, E. N. 1979 Forced and free variations of weather and climate. *J. Atmos. Sci.*, **36,** 1367–1376

Madden, R. A. 1976 Estimates of the natural variability of time-averaged sea-level pressure. *Mon. Weather Rev.*, **104,** 942–952

Nigam, S. 1990 On the structure of the observed tropospheric and stratospheric zonal-mean zonal wind. *J. Atmos. Sci.*, **47,** 1799–1813

Simmons, A. J. and Hoskins, B. J. 1978 The life cycles of some non-linear baroclinic waves. *J. Atmos. Sci.*, **35,** 414–432

Valdes, P. J. and Hoskins, B. J. 1988 Baroclinic instability of the zonally averaged flow with boundary layer damping. *J. Atmos. Sci.*, **45,** 1584–1593

Wyatt, L. R. 1981 Linear and non-linear baroclinic instability of the northern hemisphere winter zonal flow. *J. Atmos. Sci.*, **38,** 2121–2129